

Looking for the Baryon Acoustic Oscillation Signal in the 2MASS Redshift Survey Using the Wavelet Transformation

by

William Kwako

Submitted in Partial Fulfillment of the
Requirements for the Degree

Bachelor of Arts

Supervised by
Dr. Rick Watkins

Department of Physics

Willamette University, College of Liberal Arts
Salem, Oregon

2019

Presentations and publications

Kwako W., Watkins, R. (2018, September). Oral presentation as a part of Science Collaborative Research Program, Salem, OR.

Kwako W., Watkins, R. (2018, November). Poster presentation at the Murdock College Science Research Conference, Vancouver, WA.

Kwako W., Watkins, R. (2019, January). Poster presentation at 223rd Meeting of the American Astronomical Society, Seattle, WA.

Acknowledgments

Prof. Rick Watkins

Prof. Jed Rembold

Murdock Charitable Trust College Research Program for the Natural Sciences

Willamette University physics department

General Abstract

We aim to search for and analyze the baryon acoustic oscillation (BAO) signal in the 2MRS (2MASS redshift survey) using a density field created by cosmographer Brent Tully. BAOs imprint a particular pattern on the distribution of galaxies. They are characterized by a thin, hollow spherical shell of galaxies surrounding a dense core of galaxies. Utilizing a wavelet transformation, as first proposed by P. Arnalte-mur et al. in 2012, we search for the location and frequency of BAOs. We construct a wavelet - a three-dimensional hollow spherical shell with an associated density and with variable radius and width. We matched the density distribution of various regions in space with the density distribution of the wavelet. We determined the best-fit characteristics of the BAO signal to be $R = 117 \pm 11.0 h^{-1} \text{Mpc}$ and $s = 30 \pm 10.8 h^{-1} \text{Mpc}$ via the method of the wavelet transformation. We plotted radial density profile plots - plots that tell us how the density of space varies as we move away from a particular location - of our BAO signal to confirm the signal's existence. This method yielded $R = 110 h^{-1} \text{Mpc}$, corroborating results of previous studies. Lastly, we calculated the probability of the BAO signal occurring in our data set due to random distribution to be 0.0091, corresponding to $\sigma = 2.36$ away from our mean, indicating a high likelihood that our method did indeed find BAOs.

Technical Abstract

We aim to search for and analyze the baryon acoustic oscillation (BAO) signal in the 2MRS (2MASS redshift survey) using a density field created by cosmographer Brent Tully. BAOs cause thin shells of galaxies to be imprinted on the galaxy distribution; a characteristic pattern that we can search for in our dataset. Utilizing a wavelet transformation, as first proposed by P. Arnalte-mur et al. in 2012, we search for the location and frequency of BAOs. By convolving any point in our data set with a wavelet that has compact support, we create a function that returns values based on how well any region of space matches the density distribution of a BAO, with a higher value indicating a higher correlation. Identifying locations in our data set with both a high density and a high matching parameter yields points that are the most likely to correspond to BAO signals. We determined the best-fit characteristics of the BAO signal to be $R = 117 \pm 11.0 h^{-1} \text{Mpc}$ and $s = 30 \pm 10.8 h^{-1} \text{Mpc}$ via the method of the wavelet transformation, while radial density profile plots of the two BAO signals yielded a value of $R = 110 h^{-1} \text{Mpc}$, corroborating results of previous studies. We calculated the probability of the BAO signal occurring in our data set due to random distribution to be 0.0091, corresponding to $\sigma = 2.36$ away from our mean, indicating a high likelihood that our method did indeed find BAOs.

Table of Contents

Acknowledgments	iii
General Abstract	iv
Technical Abstract	v
List of Figures	vii
1 Introduction	1
2 Background	3
2.1 Isotropy and Homogeneity	3
2.2 The Scale Factor and the Expanding Universe	5
2.3 Baryon Acoustic Oscillations	7
2.4 The 2MRS and Tully's Density Field	9
2.5 The Wavelet Transformation	12
3 Method	16
3.1 Convolutions and the FFT	16
3.2 Utilizing the Wavelet Transformation	18
4 Results	19
4.1 Characteristics of the BAO Signal: R and s Parameters	19
4.2 Potential BAO Points and Radial Density Plots	19
5 Discussion	23
5.1 Error Analysis and Previous Studies	23
5.2 Significance of the BAO Discovery	24
Bibliography	25

List of Figures

- | | | |
|-----|---|----|
| 2.1 | A slice of the z-axis of the 2dFGRS showing the location of galaxies plotted against distance and right ascension [1]. Each blue dot represents a galaxy. It appears that the universe becomes less dense as redshift increases, but this is a result of only the brightest galaxies giving off distinguishable redshifts [2]. | 4 |
| 2.2 | A graph detailing the period of time the three density parameters dominated. Radiation was the first to dominate, followed by matter, and finally, vacuum energy. The vacuum energy term dominates today, leading to a universe whose rate of expansion is increasing. Time versus density parameter graphs are extraordinarily difficult to plot due to their necessary precision, so note that this graph is approximate at best, and was not created using experimental data. | 7 |
| 2.3 | An artist's representation of a BAO can be seen in the above figure [3]. Spherical shells of galaxies surround dense cores of galaxies. The density is high at the center of the dense cluster of galaxies, and as we move radially away, drastically decreases. As we pass through the spherical shell of galaxies, the density spikes, then continues to decrease. | 8 |
| 2.4 | The 2MRS map and the locations of its 44, 599 galaxies are plotted above [4]. The 2MRS uses the galactic coordinate system, a spherical coordinate system used on galactic scales. Its origin is at the sun, and has its positive direction pointing towards the center of the Milky Way. Dots toward the red side of the visible light spectrum represent a higher degree of redshift than dots toward the violet end of the visible light spectrum. The 'zone of avoidance' is present in this map, and prevents galaxies being seen in a small region along the xy-plane, centered at 0. | 10 |

2.5 These two figures are slices of Tully's density field. The figure on the left is a slice of the xy plane, and the figure on the right is a slice of the xz plane, where both slices are plotted in supergalactic coordinates. Blue clumps represent low density galaxy groups, while red areas represent higher density galaxy groups. The area in which no galaxy groups fall in the xy slice is called the zone of avoidance, created by the milky way blocking our view of far away galaxies. The zone of avoidance is not present in the other plane, as the milky way is not viewable in the other. The units of both plots are in km/s , as Tully plots the left hand side of the Hubble relation, cz , instead of directly plotting distance.	11
2.6 A depiction of a third degree B-spline. A third degree B-spline is a mathematical construction with a polynomial degree of three. They have the property of having as many continuous derivatives as is equal to their degree, and additionally have the property of compact support, enabling their function and its derivatives to go to zero at the endpoints of the interval.	15
2.7 The left image depicts the radial profile of a one-dimensional wavelet, and the right image depicts three-dimensional wavelet with a slice taken through its center. The wavelet is composed of the difference between two third degree B-splines. It thus inherits the property of compact support, creating a localized wavelet with a high density in the center surrounded by two low density areas.	15
3.1 The larger σ in our Gaussian equation is, the higher degree of smoothing is applied to our data set. The left-most image has no smoothing, the middle image some smoothing ($\sigma = 3$), and the right-most image has a high degree of smoothing ($\sigma = 5$).	17
4.1 A contour plot with an overlay of a heatmap, indicating the matching parameter values yielded by various R and s values. We found the parameters that best characterize the BAO signal to be $R = 117 \pm 11.0 h^{-1} Mpc$ and $s = 30 \pm 10.8 h^{-1} Mpc$. Uncertainties were measured by fitting a Gaussian to one-dimensional slices of our contour plot and extracting the σ value for R and s , respectively.	20
4.2 A graph of the radial density profile of the two locations yielding BAO signals. The green and blue lines each represent a BAO, and the red line is the average of both BAO radial densities. The shell of the BAO signal is apparent in both points, and occurs at the same location, $R = 110$. The width of the shell is difficult to ascertain from the radial density profile plot and relate to the values given by the wavelet transformation, so we instead focus only on R . . .	21

- 4.3 A histogram from which the likelihood to receive our results by chance can be calculated. The average matching parameter of the two BAOs in our data set was 1.89, corresponding to 2.36σ away from the mean matching parameter of zero via the fitted Gaussian, which had $\sigma = 0.8$. Thus, using this histogram, we calculate the probability of receiving our results from random chance as 0.0091. 22

1 Introduction

Observations of local regions in space have determined that celestial objects appear to recede from us. But this apparent recession is actually due to space expanding in between us and celestial bodies, only making it appear that objects are moving away. And not only is space expanding just in between us and surrounding objects, but it is expanding in between all celestial bodies. When the universe “expands,” the amount of space in areas of low density increases. Another way to think of this is the space between areas of high density increasing. A good way to visualize the idea of the expansion of space is to imagine baking a loaf of raisin bread. As the bread bakes and rises in the oven, the raisins stretch away from each other, caused by the expansion of the dough. In a similar way, as the universe expands, each galaxy gets farther and farther away from all other galaxies [2].

On large scales, we can characterize the universe as being both homogeneous and isotropic. We call the universe homogeneous because on large scales, galaxies are equally distributed; we call the universe isotropic because it is the same in all directions. Any observed region in space would look, on large scales, identical to any other observed area. We must include the addendum “on large scales,” because on smaller scales, the universe is most certainly not the same everywhere; we see a sun in one direction, a planet in another, etc. A complete understanding of the universe and its contents requires a comprehensive grasp of the universe’s distance and time scales. By breaking a seemingly massive and difficult problem into smaller tasks, we can begin to understand both scales. In this study we analyzed large-scale structure, and more specifically, a perturbation in the early universe called a baryon acoustic oscillation (BAO), whose characteristics are imprinted on the distribution of galaxies.

BAOs form in the hot, dense plasma of the early universe. While gravitational instability caused dense areas to become more dense, pressure opposed the collapsing of the regions composed primarily of dark matter, pushing outwards and creating outgoing spherical waves that dragged the baryonic matter components along with it. When the universe entered the recombination era, these spherical

waves froze in space, creating galaxies at the origin of these oscillations, as well as around the edges of the spherical waves. These formations, remnants of acoustic waves in the early universe, are called BAOs. The density at the center of the BAO signal is extraordinarily high due to the cluster of galaxies, but drastically decreases as we move radially away. The density continues to decrease as we move radially away, though increases slightly as we move through the BAO shell. The residue of these early perturbations play an integral role in corroborating the results of the flatness and geometry of the universe and can be used to determine the existence and density of vacuum energy in the dark energy model [5]. Additionally, since they are hundreds of megaparsecs across, and thus on a large enough scale to participate in the expansion of the universe, they can be used in combination with comoving coordinates to play the role of a ruler, measuring cosmological distances [6].

The data set we used to analyze the BAO signal is a density field created from the 2MASS Redshift Survey (2MRS), a catalogue of the luminosity and location of nearly 50,000 galaxies [4]. Cosmographer Brent Tully created a density field of the 2MRS, turning the data set into a collection of grid-points, each with an associated density [7]. BAOs have a particular density distribution and are imprinted on the density field, which allowed us to extract the BAO signal via a wavelet transformation. Since the wavelet transformation uses the basis of a wavepacket to give us information in both the space domain and the wavenumber, it is superior to the Fourier transformation for our purposes, and has already been used to collect information about both the location and frequency of BAOs [8]. We convolved our data set with the wavelet, which returned a dimensionless value that varied in magnitude depending on how well the density of the surrounding space matched the density distribution of the wavelet. A higher matching parameter indicated a better match, and we thus searched for locations which had both a high matching parameter and a dense epicenter [9]. Then, we used the matching parameter to locate the positions of BAOs in our data.

In our data set we found two BAOs using the method of the wavelet transformation, determining the radius of the BAO signal radius to be $R = 117 \pm 11.0 h^{-1} \text{Mpc}$, and the width of the shell to be $s = 30 \pm 10.8 h^{-1} \text{Mpc}$. Our radial density profile plot corroborated our results with $R = 110 h^{-1} \text{Mpc}$. Previous studies have shown $R = 116 h^{-1} \text{Mpc}$ and $s = 20 h^{-1} \text{Mpc}$ [9], evidence of method success.

2 Background

2.1 Isotropy and Homogeneity

Though we have a number of tools at our disposal to calculate distance to far-away objects in space, perhaps the most useful is redshift, which measure the shift in light's wavelength as it travels from distance objects. Using this relative shift, we can calculate distances between objects. There are two types of phenomena that cause redshift: the Doppler effect, and the expansion of the universe. Doppler redshift occurs when an object is moving away from a receiver and emits light. The received signal has a larger wavelength because the movement stretches the wavelength. Just as a train horn sounds higher pitched coming toward a receiver and lower pitched as it recedes, light does the same thing. As an object emitting light approaches, the photons also have their wavelength lengthened or contracted by relative motion between the observer and the emitter. General redshift is given by the quantity z ,

$$z = \frac{\lambda_{\text{observed}} - \lambda_{\text{emitted}}}{\lambda_{\text{emitted}}}, \quad (2.1)$$

where $\lambda_{\text{observed}}$ is the observed wavelength, and λ_{emitted} is the wavelength of the light at the time it was emitted. Cosmological redshift causes the same effect as Doppler redshift, but is instead due to the universe expanding while photons travel through space. Therefore, observed redshift is a combination of both Doppler redshift and cosmological redshift. Redshift surveys catalogue the magnitude of redshift of celestial objects within a sampled area and seek to increase our understanding of the composition of the universe. With an understanding of redshift and its causes, we move to isotropy and homogeneity.

The universe is both isotropic and homogeneous: the same everywhere and in all directions. On large scales, one region of space is indistinguishable from any other region. Matter is equally distributed, with no region being unique. When we observe the cosmos, we see that objects appear to be receding from us - and although this is the case, it is not that objects are receding from only us, but that all

objects are receding from every other object. To preserve isotropy and homogeneity, it must be the case that the amount of space between all objects is increasing. This expansion of space can be characterized via the Hubble constant - a value dictating the rate of expansion. The Hubble constant is $H_0 \approx 70\text{km/s/Mpc}$, though studies often yield differing values. Objects receding from us appear to be receding faster than they actually are due to the expansion of space. Redshift and the Hubble constant are related through Hubble's Law, which says that cosmological redshift is given by

$$cz = H_0 r, \quad (2.2)$$

where cz is cosmological redshift, H_0 is the Hubble constant, and r is the distance to an object. Knowing the rate of expansion of the universe is integral to calculating cosmological redshift, allowing us to relate redshift and the expansion of space, and more accurately depict cosmological scales and calculate distances to objects.

Redshift surveys confirm homogeneity: Fig. 2.1 shows a slice of the 2 degree field of view galaxy redshift survey (2dFGRS), showing a glimpse of large-scale structure. It catalogues locations and luminosities of galaxies out to two billion lightyears, corresponding to a redshift factor of 0.20, with each blue dot representing a galaxy. Although it appears that the number of galaxies present decreases as we move outwards from the origin, this is a false representation of the density of galaxies [2], as only the brightest galaxies yield distinguishable redshifts when observed from far away.

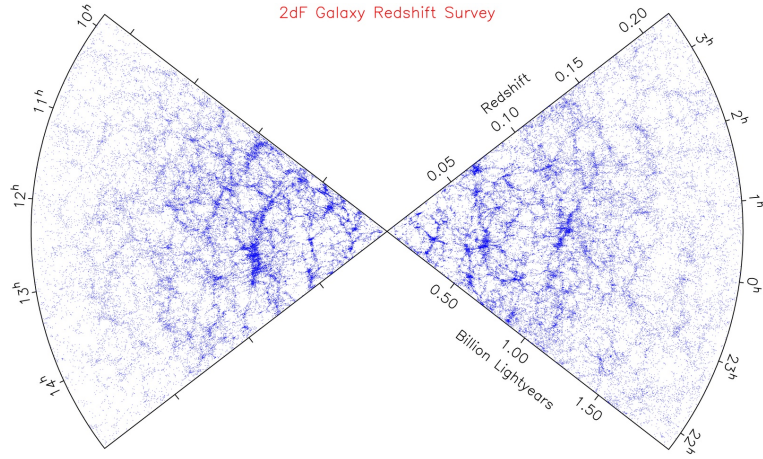


Figure 2.1: A slice of the z-axis of the 2dFGRS showing the location of galaxies plotted against distance and right ascension [1]. Each blue dot represents a galaxy. It appears that the universe becomes less dense as redshift increases, but this is a result of only the brightest galaxies giving off distinguishable redshifts [2].

The universe also possesses the property of isotropy - it is the same in all directions. Any observed area is, on large scales, indistinguishable from any other

observed area, regardless of the direction of observation. This was later corroborated by the discovery of the presence of the cosmic microwave background (CMB) [10]. The CMB is the faint, uniform, and isotropic emanation of radiation from all regions of space.

2.2 The Scale Factor and the Expanding Universe

The Big Bang happened everywhere simultaneously, sparking the existence of the cosmos. One of the most simple and useful ways to describe the expansion of the universe can be found by analyzing the scale factor, $a(t)$. It describes the expansion of the universe in a single function of time. It is dimensionless and varies between zero at the Big Bang, to one today. In addition to being a tool with which to measure time in the universe, it can also be used to measure distance. We can relate the scale factor and distance with the equation

$$r(t) = r_0 a(t), \quad (2.3)$$

where $a(t)$ is the scale factor, r_0 is the distance separating two objects in the present day, and $r(t)$ is the distance separating two objects as a function of time [2]. As $a(t)$ varies between zero and one, the distance between two objects increases. Although we can calculate distance and the rate of the expansion of the universe using the scale factor, the components that determine the shape of $a(t)$ are called density parameters. Together, the density parameters account for all the energy in the universe, and their fractions determine the rate of acceleration of the expansion of the universe.

The three types of ‘stuff’ in the universe - matter, radiation, and vacuum energy - each account for a percentage of the universe’s energy density. Since each density parameter depends on the scale factor, we can calculate how much each type of energy density contributed to the total energy density of the universe at any particular time provided the scale factor is known. ρ_m is the density of ‘cold’ matter and includes any non-relativistic matter, such as baryonic matter, dark matter, and electrons. The energy density of cold matter decreases as the universe expands by a factor of $1/a^3$. We can think of the reason why the energy density falls off in this way by imagining a box of particles. If we expand the box by the same amount on all sides, the density falls off like $1/a$ for each dimension - corresponding to a ratio of $1/a^3$ for three dimensions. The energy density of radiation and relativistic particles, ρ_r , decreases in a similar way, but has an extra factor of $1/a$ due to the redshift of photons further decreasing its energy. Lastly, ρ_Λ represents the energy density of “dark energy,” a mysterious substance whose energy density stays constant, regardless of the size of the universe. Other

than knowing that it in some way contributes to structure formation and that its energy density does not vary with time, very little is known about dark energy. The three densities can thus be defined as being proportional to the scale factor in the following equations [2]:

$$\rho_m \propto 1/a^3, \quad (2.4)$$

$$\rho_r \propto 1/a^4, \quad (2.5)$$

$$\rho_\Lambda \propto 1. \quad (2.6)$$

Today, ρ_m accounts for $\approx 27.26\%$ of the total energy density, of which 22.70% is dark matter [2]. ρ_r holds $\approx 0.0084\%$ of the total energy in the universe, and dark energy accounts for the rest, almost 73% [2].

In Fig. 2.2, we can see an approximate evolution of the density parameters according to the scale factor. Because the radiation density parameter goes like $1/a^4$, it will be larger than ρ_m for small a . For larger a , matter will begin to dominate, and finally, when a is large enough, both the radiation and matter terms fall off and the vacuum energy term will be the largest, as it is constant. During both the radiation and matter dominated eras, the universe's rate of expansion was decreasing. It is only during the vacuum energy dominated era that the universe's rate of expansion increases. The universe began with a set of initial conditions, including an initial temperature and size, as well as other observable properties that have evolved throughout the universe's history. As the universe expands, the amount of total energy density that each density parameter represents changes. With the domination of different density parameters, the properties of the universe change.

Both the radiation-dominated and matter-dominated eras are the most important to understanding our research. The first major epoch was one in which the radiation density parameter dominates, and lasted approximately 72,000 years. Although radiation accounts for a small percentage of the energy density of the universe today, ρ_r was the dominating parameter when the universe was young. The universe was dense and hot, causing the vast majority of particles to be relativistic [2]. As the radiation era came to a close, matter became the dominating density parameter. This era lasted for almost eight billion years - the majority of the universe's existence. But near the beginning of the start of this era, when the universe was approximately 300,000 years old, the universe underwent an important event called recombination. Until recombination, the universe was so hot and dense that baryonic matter and radiation were ionized and coupled - they were inseparable and had to move together. The beginning of the recombination epoch is marked by the temperature dropping significantly enough to allow matter to form bonds and create neutral hydrogen. Photons interact with charged particles but not with neutral hydrogen, so as hydrogen begins to form, photons and matter decouple [2], causing the universe to become transparent. The creation of

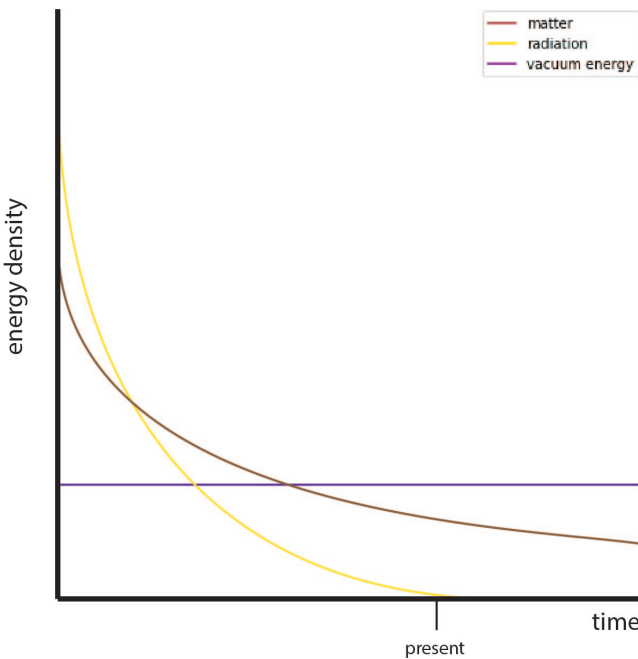


Figure 2.2: A graph detailing the period of time the three density parameters dominated. Radiation was the first to dominate, followed by matter, and finally, vacuum energy. The vacuum energy term dominates today, leading to a universe whose rate of expansion is increasing. Time versus density parameter graphs are extraordinarily difficult to plot due to their necessary precision, so note that this graph is approximate at best, and was not created using experimental data.

Hydrogen signifies the beginning of large-scale structure formation, leading to the formation of stars and galaxies.

As the age of the universe increases, it slowly became less uniform over smaller scales due to gravity. As the universe stretched, gravity pulled matter out of low density regions and into higher density regions. Thus, overdense regions became increasingly overdense, while underdense regions became increasingly underdense. This is known as gravitational instability, and lead to the formation of galaxies at overdense regions. Underdense regions emptied themselves of all mass, forming vast regions of empty space called voids. Since gravitational instability is omnipresent, galaxies all formed at the same time in similar regions of overdensity.

2.3 Baryon Acoustic Oscillations

Before recombination, gravitational instability compressed regions of overdensity into dense clumps of matter, dark matter, and radiation. If these clumps were compressed too much, however, trapped radiation pressure would push outwards

against the force of gravity, causing an expansion rather than a contraction. Gravity and pressure continuously opposed each other, creating oscillating clumps of mass throughout the entirety of the history of the early universe. As a clump expanded, the radiation-driven expansion would drag baryonic matter along with it, pushing matter to the perimeter of the clump, causing the clump to expand in the form of a hollow spherical shell.

When recombination occurred, the clump collapsed in on itself due to the presence of large amounts of dark matter unable to interact with the other components of mass and the outgoing waves of radiation, and baryonic matter froze in place in the shape of a hollow spherical shell. As the shell pulled in dark matter, and the dark matter at the center pulled in baryonic matter, the conditions necessary for structure formation were satisfied, and galaxies formed. The end result is a dense cluster of galaxies at the origin of these oscillations, with a hollow shell of galaxies surrounding the dense epicenter [9]. An artist's representation of the galaxies that produce this distribution can be seen in Fig. 2.3. At the center, a dense core of galaxies, and farther away, a spherical shell of galaxies. This structure is called a baryon acoustic oscillation (BAO).

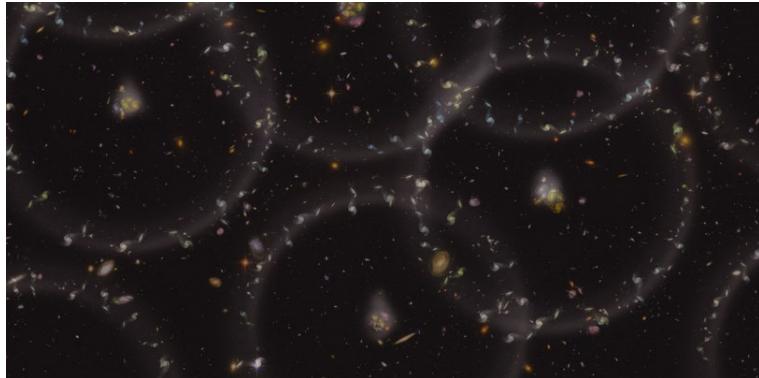


Figure 2.3: An artist's representation of a BAO can be seen in the above figure [3]. Spherical shells of galaxies surround dense cores of galaxies. The density is high at the center of the dense cluster of galaxies, and as we move radially away, drastically decreases. As we pass through the spherical shell of galaxies, the density spikes, then continues to decrease.

Both the epicenter of a BAO signal and its surrounding shell of galaxies are areas of overdensity. Thus, if we were to model the density as we move radially away from the center of a BAO signal, we would see a spike in density at the center, and a sharp decrease as we moved radially away, with an additional increase in density as we moved through the shell of galaxies. We are able to model the BAO signal using a spherical shell of constant density. In this model, the BAO can be parameterized in terms of the radius of the sphere, R , and the width of its shell, s .

The size of BAOs have been observed to be on the scale of hundreds of Mpc - large enough to participate in the expansion of the universe. We can use a combination of an observed BAO and its theoretical model to trace BAOs back to their origins, corroborating the scale factor and the geometry of the universe [5] [6]. Additionally, the distance between two BAOs can be determined by calculating the difference between their radii, and by using the rate of the expansion of the universe. There have been many methods previously employed to detect BAOs: identifying patterns in dark matter to look for BAOs using the Lyman- α forest [11]; finding the imprinted BAO signal in the power spectrum [12]; and using the wavelet transformation to “filter out” the non-BAO data [9]. We will be using this last method to search for BAOs, analyzing their frequency and location in Tully’s density field, created from the 2MASS Redshift Survey [7] [4].

2.4 The 2MRS and Tully’s Density Field

The 2MASS Redshift Survey (2MRS) is a catalogue of the position and luminosity of almost 50,000 galaxies [4]. It is a redshift survey that aims to create a three-dimensional map of all galaxies in the nearby universe by using galactic coordinates, a spherical coordinate system with its origin at the sun and the equatorial plane being the plane of the galaxy [4]. This coordinate system excels at marking locations at the galactic level. A map of the galaxies located by the 2MRS can be seen in Fig. 2.4. Each color represents a varying magnitude of redshift, denoted by the color bar on the bottom right of the figure. An interesting note to make about this map is the lack of galaxies around zero on the xy-plane. If we look directly into the Milky Way Galaxy, it becomes extremely difficult to distinguish galaxies through the light pollution and haze of star clusters in the way. Thus, this titled ‘zone of avoidance’ will be present on any galactic map that takes data from a location within the Milky Way.

Cosmographer Brent Tully created a density field from the 2MRS that was vital to conducting this research [7]. He finds collections of galaxies, known as galaxy groups, then turns the spanning area of the 2MRS into a density field, using the location and size of each galaxy group as a guide. Normally, determining which galaxies fall into which galaxy groups is a difficult task due to the innate inaccuracy generated using redshift as a means to calculate distance. This so-called redshift distortion causes velocities to affect the distance assigned to objects through their redshifts. In making the density field. Tully makes several corrections that attempt to minimize redshift distortion, thus reducing error in forming galaxy groups.

Although the 2MRS gives the luminosity of galaxies and not the mass, Jacob K. E. Halm discovered that mass and luminosity have a direct linear relationship, thus allowing us to classify galaxies that have a higher luminosity as also having a higher

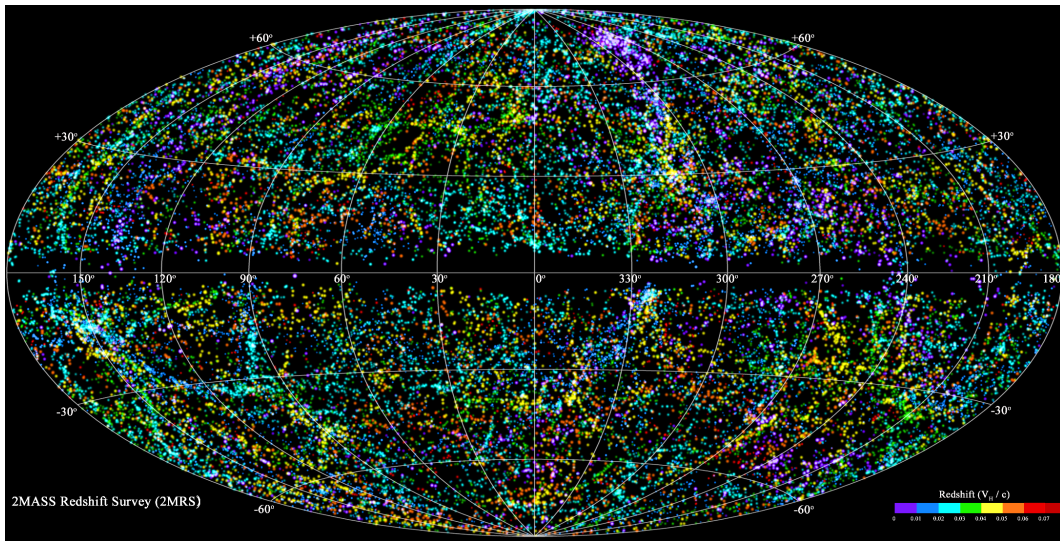


Figure 2.4: The 2MRS map and the locations of its 44,599 galaxies are plotted above [4]. The 2MRS uses the galactic coordinate system, a spherical coordinate system used on galactic scales. Its origin is at the sun, and has its positive direction pointing towards the center of the Milky Way. Dots toward the red side of the visible light spectrum represent a higher degree of redshift than dots toward the violet end of the visible light spectrum. The ‘zone of avoidance’ is present in this map, and prevents galaxies being seen in a small region along the xy-plane, centered at 0.

mass [13]. Tully flux-limits his density field, meaning that he only catalogues galaxies with a minimum amount of flux. To account for the flux lost by observing objects that are far away, Tully adds flux to detected galaxies based on their distance [7]. He uses a group-finding algorithm that is based on the most likely distance galaxies are away from each other in any particular galaxy group. He applies his group-finding algorithm to the most luminous galaxy first and finds other nearby galaxies. Each galaxy found to be within a satisfactory distance of the most luminous galaxy also has the group-finding algorithm applied to them. This process is repeated until no new galaxies are found, at which point he repeats the process, but starts with the next luminous galaxy in the data set. Lastly, Tully finds the total mass in each galaxy group, then splits the density field into grid-points, with each grid-point possessing an associated density. While the 2MRS is spherically shaped, Tully creates the density field in the shape of a cube, with each side length being 400Mpc in length. Note that although the density field has more area, it is still a direct mapping of the 2MRS, and thus the corners have no observable galaxy groups [7] [4].

Two slices of Tully’s density field can be seen in Fig. 2.5, where a ‘slice’ fixes one variable in a three-dimensional system while letting the others vary, causing a

two-dimensional projection of a three-dimensional space. The image on the left is a slice in the xy plane, and the image on the right is a slice in the xz plane. Each clump in each slice represents a galaxy-group, with bluer clumps being less dense than redder ones. Our solar system is located at the center of the 2MRS and thus, the density field, which the resolution appears to change as deviate farther from the center. As we observe objects farther away, only the brightest objects yield distinguishable redshifts. Tully uses units of km/s to plot the density field, which comes from the Hubble relation, equation 2.2. The left side of equation 2.2 is plotted, hence the units km/s along the axes. Since the exact value of H_0 is not agreed upon, plotting cz instead of r acts as a way of plotting the axes in units that do not depend on knowing the true value of H_0 .

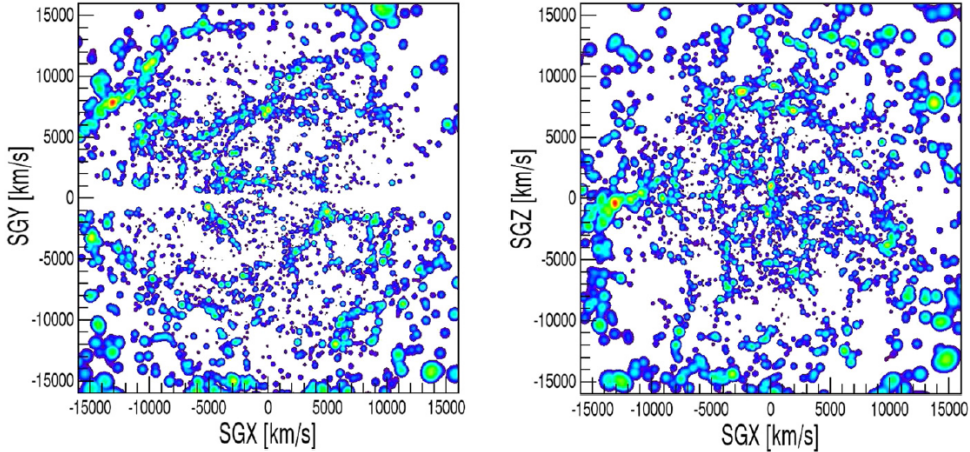


Figure 2.5: These two figures are slices of Tully’s density field. The figure on the left is a slice of the xy plane, and the figure on the right is a slice of the xz plane, where both slices are plotted in supergalactic coordinates. Blue clumps represent low density galaxy groups, while red areas represent higher density galaxy groups. The area in which no galaxy groups fall in the xy slice is called the zone of avoidance, created by the milky way blocking our view of far away galaxies. The zone of avoidance is not present in the other plane, as the milky way is not viewable in the other. The units of both plots are in km/s , as Tully plots the left hand side of the Hubble relation, cz , instead of directly plotting distance.

Although each data point in Tully’s density field is given in terms of density, we worked in terms of the density contrast,

$$\delta(\mathbf{r}) = \frac{\rho(\mathbf{r}) - \rho_0}{\rho_0}, \quad (2.7)$$

where $\rho(\mathbf{r})$ is the density of a particular point in the data set, and ρ_0 is the average density of the data set. Conceptually, the density contrast gives the difference

from the average density in terms of the average density. Working with this type of density field is much easier than working with any other form of data as the density contrast is a dimensionless parameter with a zero average that neatly describes the density field. Since we are looking for a particular distribution of matter, the BAO signal is imprinted on the data, thus making it easier to identify and analyze their frequency and location. We now describe our method that we used to identify BAOs.

2.5 The Wavelet Transformation

Before jumping right into what a wavelet is, we will first give some background about linear algebra to get the reader accustomed to the notation and intuitive meaning behind the wavelet transformation. An in-depth view of linear algebra would be overwhelming and would dilute the purpose of this section with excessive theory and notation, so we will instead be focusing on the most crucial aspects necessary to understand the mathematics behind the wavelet transformation. As such, this will be an extremely informal introduction to linear algebra.

The three-dimensional Cartesian coordinate system uses the variables x , y , and z , each of which represent one of the three dimensions. Thus, a vector \mathbf{v} can be written as

$$\mathbf{v} = v_x \hat{x} + v_y \hat{y} + v_z \hat{z}, \quad (2.8)$$

where we have broken up the vector into its components in each direction multiplied by a unit vector in the same direction. We can express any vector in the Cartesian plane as a column vector - a 3×1 matrix in which each row represents each dimension. Therefore, we write it in the form

$$\mathbf{v} = v_x \begin{bmatrix} 1 \\ 0 \\ 0 \end{bmatrix} + v_y \begin{bmatrix} 0 \\ 1 \\ 0 \end{bmatrix} + v_z \begin{bmatrix} 0 \\ 0 \\ 1 \end{bmatrix}, \quad (2.9)$$

where each unit vector has been broken into its own column vector. Equations (2.8) and (2.9) are different ways of representing the same vector. More explicitly, we broke our unit vectors into their column vectors, formally represented by

$$\hat{x} = \begin{bmatrix} 1 \\ 0 \\ 0 \end{bmatrix}, \quad \hat{y} = \begin{bmatrix} 0 \\ 1 \\ 0 \end{bmatrix}, \quad \hat{z} = \begin{bmatrix} 0 \\ 0 \\ 1 \end{bmatrix}. \quad (2.10)$$

Every possible three-dimensional vector in the Cartesian plane can be characterized with some combination of the above \hat{x} , \hat{y} , and \hat{z} vectors. Stated another way,

if we are allowed to multiply \hat{x} , \hat{y} , and \hat{z} by any scalar, there is no constraint to what the vector \mathbf{v} is allowed to be. If this property holds, we formally say that \hat{x} , \hat{y} and \hat{z} vectors *span* the set of all three-dimensional Cartesian coordinates [14]. Each vector \mathbf{v} in the three-dimensional Cartesian coordinate system has a unique representation of these \hat{x} , \hat{y} , and \hat{z} vectors [14].

There is an additional property of the above spanning vectors in (2.10): none of the vectors can be created with vectors in the spanning set. For example, \hat{x} cannot be created with any linear combination of \hat{y} and \hat{z} vectors, and the same applies to \hat{y} and \hat{z} . Thus, we say that \hat{x} , \hat{y} , and \hat{z} are *linearly independent* [14]. When a set of vectors satisfy these properties - that is, they both span their vector space and are linearly independent, we call them a *basis* [14]. This idea of a basis is extremely important and comes up all over the place in most areas of physics. An additional property of the above basis vectors, that need not be satisfied but is in this case, is the property of orthogonality. Two vectors are said to be orthogonal if their dot product is identically zero [14].

This idea of orthogonal basis vectors can be extended to all coordinate systems - it need not be restricted to Cartesian. Polar, cylindrical, and spherical coordinates all have basis vectors which are both linearly independent and span their vector spaces. Additionally, we can generalize the notion of building any vector out of the sum of linear basis vectors to include functions as well. Modeling a function as a vector whose dimensions are infinite, we can extend the notion of span and linear independence to functions. That is, we can build any function out of a set of basis functions. Fourier transformations use $\sin x$ and $\cos x$ as basis functions to model other functions, allowing the decomposition of a function into a sum of only $\sin x$ and $\cos x$ components. As a real world example, if we start with a mixed bucket of paint, performing a Fourier transform allows us to determine what colors, and how much of each color, went into creating the mixed bucket of paint. Although the Fourier transformation can be written in terms of $\sin x$ and $\cos x$ functions, it can also be thought of in terms of exponentials. The continuous Fourier transform is given by

$$\hat{g}(k) = \int_{t_1}^{t_2} g(x)e^{-2\pi i k x} dt, \quad (2.11)$$

where $\hat{g}(k)$ is the representation of the function in the wavenumber domain, $g(x)$ is the representation of the function in the spatial domain, k is the wavenumber, and x is the spacial component. The idea of basis functions as opposed to basis vectors, like in the case of the Fourier transformation, is perhaps the most similar to the idea behind the wavelet transformation.

The wavelet transformation can be succinctly summarized by saying that it is simply a change of coordinates to a different set of basis functions. It uses a wave packet, a localized collection of superimposed waves, as a basis function [8]. And

unlike the Fourier transformation, it gives information in both the space domain and the wavenumber domain, allowing us to identify the location and frequency of any function to which we apply it [8]. Wavelets are often used to deconstruct data into components of frequency or wavenumber, which can then be analyzed. They see use often in image compression, musical analysis, quantum mechanics, and seismology [15]. An example of a function that generates wavelets is the following:

$$\psi_{s,l}(x) = 2^{-\frac{s}{2}} \psi(2^{-s}x - l), \quad (2.12)$$

where $\psi_{s,l}(x)$ is the wavelet basis, and ψ is a function of s , x , and l , changing based on those parameters [15]. The way in which we use wavelet transformations is most unorthodox. Instead of using it to analyze components of frequency or wavenumber, we instead create a three-dimensional wavelet that is able to model the characteristic parameters of the BAO signal. We begin with wave packets which have the radial profile

$$\psi_{R,s}(r) = \frac{\alpha_{R,s}}{4\pi r^2} \left[2B_3\left(2\frac{r-R}{s}\right) - B_3\left(\frac{r-R}{s}\right) \right], \quad (2.13)$$

where R and s are the parameters that characterize the BAO, $\alpha_{R,s}$ is the normalization constant, and $B_3(x)$ is the box spline of the third degree,

$$B_3(x) = \frac{1}{12} (|x-2|^3 - 4|x-1|^3 + 6|x|^3 - 4|x+1|^3 + |x+2|^3). \quad (2.14)$$

A B-spline is a basis function composed of multiple polynomials. The number of continuous derivatives of the B-spline is equal to its degree. Thus, our B-spline of the third degree has three continuous derivatives, while all derivatives above the third are equal to zero. We need our B-spline function to be a third degree polynomial to create the desired shape of the wavelet. In Fig. 2.6, we depict a third degree B-spline function. Our function has compact support, meaning that it and its derivatives go to zero at the endpoints of the interval.

Our wavelet is composed of two different B-spline functions subtracted from each other, allowing our wavelet to inherit the property of compact support. Additionally, its integral is zero. The idea behind using a wavelet transformation is that it is a localized function, so having a wavelet go to zero in a finite space is an extremely important property that makes mathematical calculations significantly easier. In Fig. 2.7, we display two images of the same wavelet. The left image is the radial profile of a one-dimensional viewing of a wavelet, and the right image is a slice of a three-dimensional wavelet. Using the colorbar on the far right as a key for interpreting the three-dimensional wavelet, we can see that the dark green ring has the highest magnitude, with the inner and outer white rings representing negative values. The rest of the area is of average magnitude. This particular wavelet has $R = 100h^{-1}\text{Mpc}$ and $s = 20h^{-1}\text{Mpc}$.

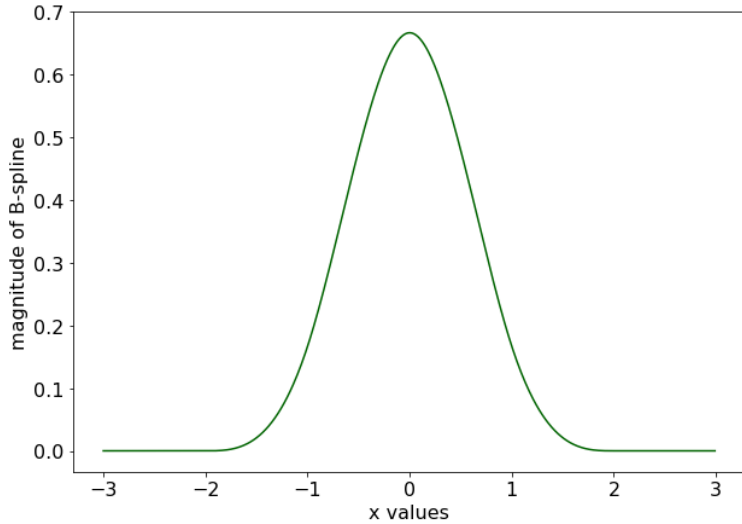


Figure 2.6: A depiction of a third degree B-spline. A third degree B-spline is a mathematical construction with a polynomial degree of three. They have the property of having as many continuous derivatives as is equal to their degree, and additionally have the property of compact support, enabling their function and its derivatives to go to zero at the endpoints of the interval.

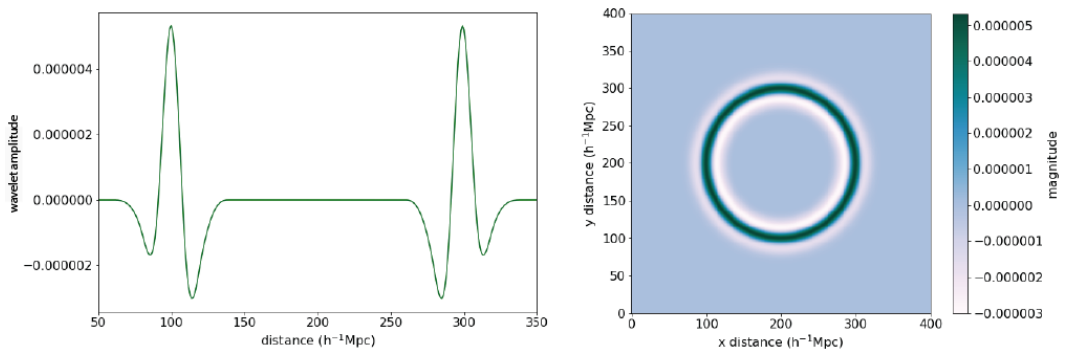


Figure 2.7: The left image depicts the radial profile of a one-dimensional wavelet, and the right image depicts three-dimensional wavelet with a slice taken through its center. The wavelet is composed of the difference between two third degree B-splines. It thus inherits the property of compact support, creating a localized wavelet with a high density in the center surrounded by two low density areas.

3 Method

3.1 Convolutions and the FFT

BAOs imprint a unique pattern on the density field in which we are searching. As discussed earlier, they are characterized by dense epicenters, surrounded by a spherical shell of galaxies. Although the entire volume of the BAO is an area of overdensity, there is an abrupt spike in density at the spherical shell. Using this distribution of density and the previously discussed wavelet transformation, we were able to identify locations in our data set that corresponded to locations of BAOs. The key to obtaining these locations was to make use of a convolution: a mathematical operation that takes two functions and returns a third which expresses how one function affects the other. A convolution is given by the equation

$$(f * g)(x) = \int_{-\infty}^{\infty} f(y)g(y - x)dy, \quad (3.1)$$

where f and g are the two functions being convolved, $(f * g)$ represents the convolved function, y is our spatial variable, and x is a shifting parameter. The shifting parameter places one function on top of the other at every point in space, and the integral calculates the amount of overlap between the two functions. The above equation, however, is difficult to work with and time consuming to calculate, so instead of convolving functions in the spatial domain, we shift to the wavenumber domain, in which convolutions are significantly easier to perform. Recall that, as discussed above, a Fourier transformation on a function in the spacial domain takes it to the wavenumber domain. The convolution theorem states

$$\mathcal{F}(f * g) = \mathcal{F}(f) \cdot \mathcal{F}(g), \quad (3.2)$$

where \mathcal{F} is the Fourier transform operator and performs a Fourier transform on a function, taking it to frequency-space [16]. Rearranging this equation gives us

$$(f * g) = \mathcal{F}^{-1}(\mathcal{F}(f) \cdot \mathcal{F}(g)). \quad (3.3)$$

Thus, multiplying two functions in the wavenumber domain performs a convolution, which is then brought back to the spacial domain via an inverse Fourier transform. Performing convolutions in this way is significantly easier, and can be made even faster using FFT (fast Fourier transform) algorithms. Although we let Python calculate FFTs for us, we have to be cautious when using the FFT algorithm, as byproducts of the transform bleed into the edges of our data set, giving us artifacts in our results. As a remedy, we zero pad our box so these artifacts do not affect our data, and throw away the zero-padded area after our convolution has finished.

Often, convolutions are used in conjunction with Gaussian functions to produce smoother data sets. For example, convolving our data set with a Gaussian function of the form

$$f(r) = \frac{1}{\sigma\sqrt{2\pi}} e^{\frac{-r^2}{2\sigma^2}}, \quad (3.4)$$

where $r = \sqrt{x^2 + y^2 + z^2}$ with each coordinate point in our data set being represented by an x , y , and z value, will yield a density field which appears more smooth. We perform the convolution and show the results in Fig. 3.1. Each image is of the same region of space, but with a different amount of smoothing applied. The amount of smoothing is determined by the value of σ in our Gaussian equation. The greater the σ , the more smoothing occurs when our data set is convolved with the Gaussian equation. In the left-most image, no smoothing is applied; in the middle image, $\sigma = 3$; in the far-right image, $\sigma = 5$. As σ increases, we can see that areas of high density begin to enlarge and blur together. Smoother data sets

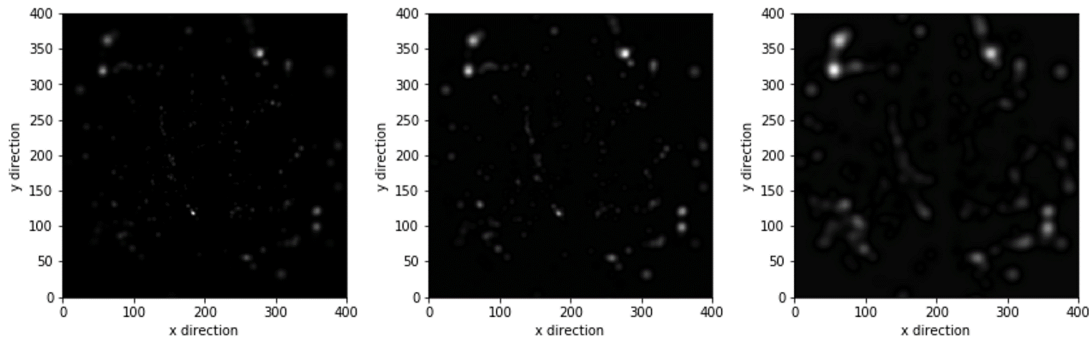


Figure 3.1: The larger σ in our Gaussian equation is, the higher degree of smoothing is applied to our data set. The left-most image has no smoothing, the middle image some smoothing ($\sigma = 3$), and the right-most image has a high degree of smoothing ($\sigma = 5$).

cause points of local maxima to become more pronounced, allowing us to more easily constrain our data in the search for BAOs.

3.2 Utilizing the Wavelet Transformation

We perform a convolution with a single point in our data set and the wavelet, giving us the equation for a wavelet transformation [9]:

$$W_{R,s}(\mathbf{x}) = \int_{\mathbb{R}^3} \psi_{\mathbf{R},s}(\mathbf{y}) \delta(\mathbf{y} - \mathbf{x}) d^3\mathbf{y}, \quad (3.5)$$

where $W_{R,s}$ is the wavelet transformation, \mathbb{R}^3 and d^3 represent integrating over all space, ψ is the wavelet with variables R and s , and δ is the density contrast. The wavelet transform of a single location in our data set yields a dimensionless matching parameter, with a positive value representing a positive correlation between the density of the wavelet and the surrounding space it is convolved with, while a negative value represents a negative correlation between the density of the wavelet and the surrounding space it is convolved with. Thus, the matching parameter tells us the amount of overlap between the density distribution of the wavelet and the density of the region the wavelet picks out. Using the method of the wavelet transformation, we first determined the R and s that best characterize the BAO signal, then determined the frequency of BAOs in our data set.

Due to the homogeneity and isotropy of the universe and the mathematical properties of the wavelet (namely, the fact that its integral is zero), the average matching parameter across all-space will be zero [9]. Furthermore, this holds even with the prevalence of BAO signals in our data set [9]. However, we can constrain our selection of data points to analyze by focusing solely on high-density locations, and are allowed to safely throw out all other points because we know that BAOs must have dense epicenters. After constraining our data set in this way, a correctly-fitted wavelet will be able to pull out the BAO signal, allowing us to detect points around which a BAO signal exists. The BAO signal begins to influence the average matching parameter as we get closer and closer to the parameters that characterize the BAO signal. Therefore, the R and s that yield the highest matching parameter when averaged around all density locations will be the R and s that characterize the BAO signal.

Determining the parameters wavelet that best fits the BAO signal then allowed us to determine locations of BAOs. Since BAOs must have a dense epicenter, we search for points with both a high matching parameter and a high density. We created a Python script capable of returning to us locations of local maxima, which was done by determining which points had densities larger than their neighbors. After setting both a density threshold and a matching parameter threshold, we were able to filter through uninteresting locations, and arrived at a handful of potential BAO locations.

4 Results

4.1 Characteristics of the BAO Signal: R and s Parameters

Proceeding under the assumption that the R and s values that successfully characterize the BAO signal will be those that yield the highest average matching parameter among all high-density coordinate points above a certain threshold, we computationally check various combinations of R and s values. A contour plot and heat map of tested R and s values can be seen in Fig. 4.1. On the x-axis we have the shell width, s , and on the y-axis, the radius, R . Both R and s are measured discretely in steps of one and are in units of megaparsecs. We found the highest average matching parameter to occur at $R = 117 \pm 11.0 h^{-1} \text{Mpc}$ and $s = 30 \pm 10.8 h^{-1} \text{Mpc}$, with uncertainties found by fitting one-dimensional Gaussian plots to slices of our contour plot, either corresponding to R , or s , respectively.

4.2 Potential BAO Points and Radial Density Plots

After finding a wavelet with the parameters that successfully characterize the BAO signal, we searched for locations of BAOs in our data set. We found eight points that potentially corresponded to locations of BAOs, and plotted their radial density profiles to confirm. A radially density profile plot tells us how the density of a location in space varies as we move radially away from it. It is an alternative way to determine BAO locations, but only yields useful information when sampling over a small collection of points. Averaging the radial profile of more than a few points distorts the BAO signal by adding noise, and manually plotting and analyzing each plot is far too much work, but doable if working with a small pool of locations.

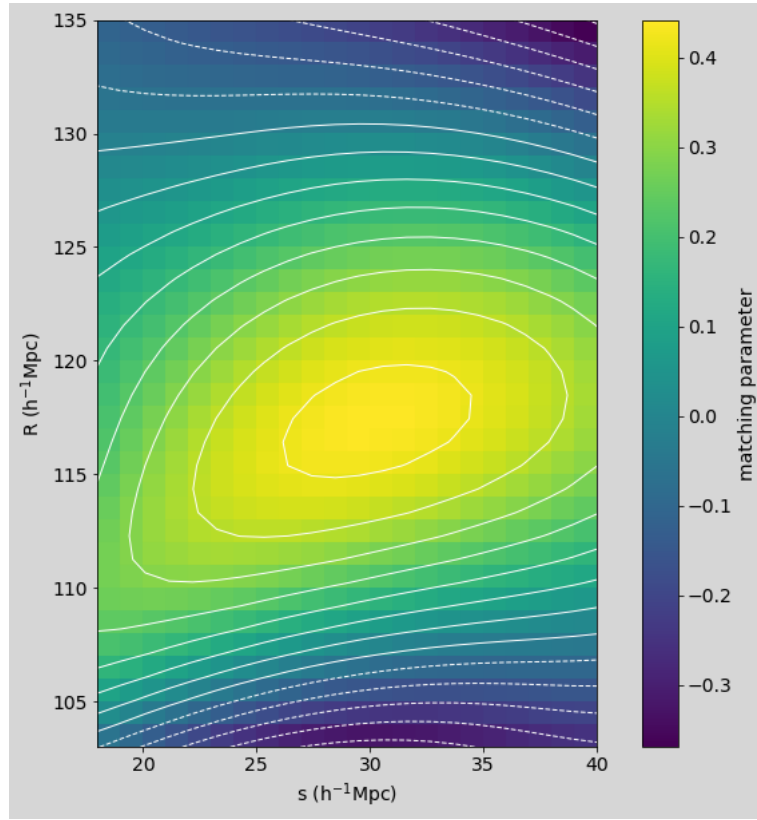


Figure 4.1: A contour plot with an overlay of a heatmap, indicating the matching parameter values yielded by various R and s values. We found the parameters that best characterize the BAO signal to be $R = 117 \pm 11.0 h^{-1} \text{Mpc}$ and $s = 30 \pm 10.8 h^{-1} \text{Mpc}$. Uncertainties were measured by fitting a Gaussian to one-dimensional slices of our contour plot and extracting the σ value for R and s , respectively.

We manually analyzed each radial density profile plot of the eight candidate points, throwing out those that had dense centers and high matching parameter values but whose shape did not match the BAO signal. Although all eight locations had both a high density and a high matching parameter value, only two ended up being legitimate signals and had the signature ‘‘BAO bump,’’ signifying a density increase at the location of the shell. We ruled out the other points based on the location of the spike in density, the width of the spikes, and difference between relative shapes of the points. These two locations had the density spike occur at the location we expected the shell to occur based on the wavelet transformation, and looked almost identical in nature. We plot the radial profiles of both locations in Fig 4.2. The green line represents the radial density profile of the first BAO point, the blue line represents the second, and the red is the average of both. The spike from the density of the shell can clearly be seen in both BAO points, with a

maximum density of the shell occurring at $R = 110 h^{-1} \text{Mpc}$ for both BAO points.

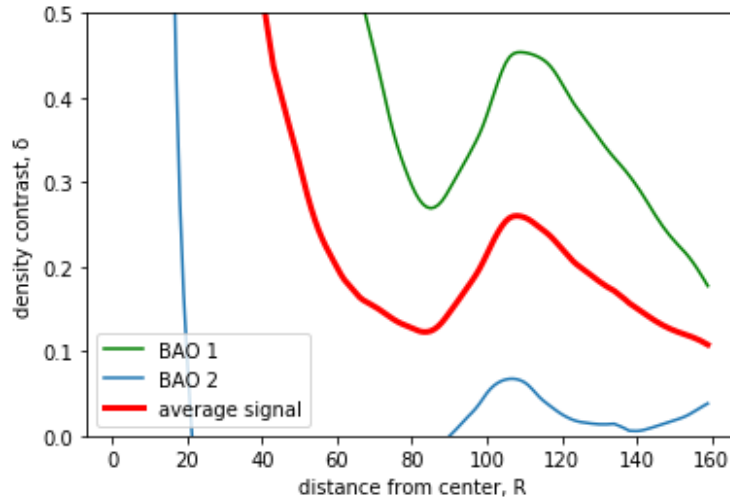


Figure 4.2: A graph of the radial density profile of the two locations yielding BAO signals. The green and blue lines each represent a BAO, and the red line is the average of both BAO radial densities. The shell of the BAO signal is apparent in both points, and occurs at the same location, $R = 110$. The width of the shell is difficult to ascertain from the radial density profile plot and relate to the values given by the wavelet transformation, so we instead focus only on R .

The wavelet transformation and the radial density profile graphs are two different methods to determine at which locations the BAO signal occurs - the R and s of BAOs for both methods need not be identical. In addition to calculating the uncertainty values of the parameters given via the wavelet transformation, we also determined how likely it is to detect a BAO signal, sampled from two random points in our data set. This determined how likely it is that the two BAO signals we detected were from coincidence and not due to the presence of real BAOs. We sample two random points in our data set 10,000 times and calculated the average matching parameter of each pair. Our histogram of this data can be seen in Fig. 4.3. We plotted a Gaussian curve on top of our histogram and determined the Gaussian to have $\sigma = 0.8$. Thus, the average matching parameter of our two BAO points, $W = 1.89$, corresponds to a 2.36σ deviation from zero, giving us a 0.0091 chance of receiving our results by chance.

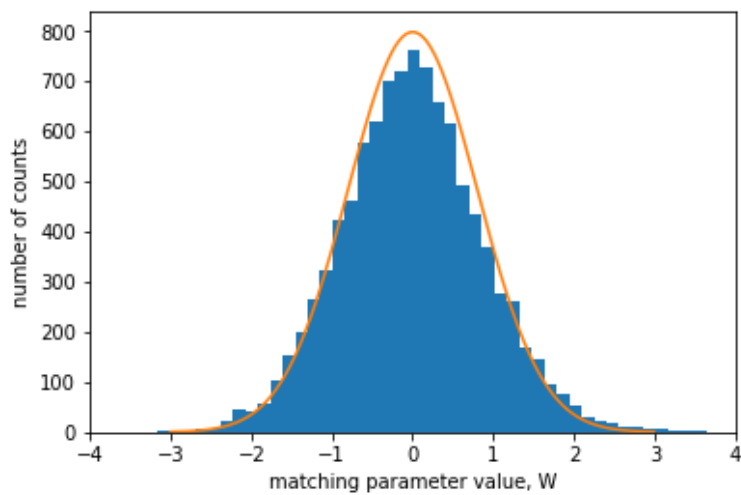


Figure 4.3: A histogram from which the likelihood to receive our results by chance can be calculated. The average matching parameter of the two BAOs in our data set was 1.89, corresponding to 2.36σ away from the mean matching parameter of zero via the fitted Gaussian, which had $\sigma = 0.8$. Thus, using this histogram, we calculate the probability of receiving our results from random chance as 0.0091.

5 Discussion

5.1 Error Analysis and Previous Studies

We found the wavelet transformation gave us characterizing parameters of $R = 117 \pm 11.0\text{h}^{-1}\text{Mpc}$ and $s = 30 \pm 10.8\text{h}^{-1}\text{Mpc}$, while the radial density profile gave us $R = 110\text{h}^{-1}\text{Mpc}$ for both points. We do not calculate the width of the BAO signals from the radial density profiles, as it is not straightforward to discern the width of the shell given the radial density profile and relate back to the characteristics of the wavelet transformation. This does not pose a current issue, as the location and shape of the BAO signal from the radial density profile plots gives us enough information to determine the locations of BAOs.

Figure 4.3 can be used to determine the probability that two random points in our data set produce the same signal as the two BAOs we found. Given our data, this probability came out to 0.0091, or a 0.91% chance of our results being duplicated due to random chance, corresponding to 2.36σ away from our mean. This result is above 2σ , meaning our values have a high probability of not being due to random chance, though we had hoped for a result closer to 4σ .

In a previous study by P. Arnalte-Mur, the characterizing parameters of a BAO were found to be $R = 116\text{h}^{-1}\text{Mpc}$ and $s = 36\text{h}^{-1}\text{Mpc}$ [9]. Since our results were $R = 117 \pm 11.0\text{h}^{-1}\text{Mpc}$ and $s = 30 \pm 10.8\text{h}^{-1}\text{Mpc}$, and our uncertainties within two standard deviations, our study corroborates his results. In addition, P. Arnalte-Mur was not able to discern the BAO signal given a single data point, instead relying on the average of multiple to produce a detectable “BAO bump.” Figure 4.2 shows radial profile densities of individual data points, indicating strong correlations with the BAO signal.

Although both the wavelet transformation and the radial density profile plots were successful in detecting BAO signals, there is room for improvement in our methods. Clearly, the wavelet transformation is able to detect BAO signals amidst noise, but it does not do so as accurately as we would like. Plotting the radial density profile of individual points is a more accurate method to detect the radius

of a BAO, since the density spike from the shell is able to be visualized, unlike the parameters generated from the wavelet transformation. Although the radius given by the wavelet transformation is within two standard deviations of the one given by the radial density profile, under ideal circumstances, the two would be equal. We propose that the wavelet transformation can be made more accurate by using a new wavelet. It would still have to be constrained such that it has the property of compact support, but perhaps it would be worth experimenting with new wavelets to see if the BAO signal can be better modeled. However, determining the characterizing parameters of the signal using the wavelet transformation is likely to always produce innate uncertainty due to the noise generated from sampling large amounts of data.

The 2MRS is considered a smaller redshift survey at 44,599 galaxies sampled, compared to others such as the 2dFGRS (232,155 galaxies) and the SDSS's BOSS, whose 10th data release catalogues over 670,000 galaxies [1] [17]. Since the diameter of the BAO signal is over half the length of the 2MRS, we are seriously constrained in where we can look for the signal. The matching parameter of locations near the edge of the data set will have a greater amount of noise due to the convolution bleeding into the area outside the confines of the data set. It is possible that there were BAO signals toward the edge of the data set that were not recognized as such due to the small sampling space of the 2MRS. It is perhaps for this reason that the 2MRS has not been analyzed for BAOs until this study. Despite the constraints, however, we were still able to detect BAO signals closer to the center of the data set - an incredible feat.

5.2 Significance of the BAO Discovery

As mentioned previously, BAOs can be used as a standard ruler, and can additionally corroborate the theory of dark matter and the standard model of cosmology. By comparing the relative radii of two observed BAOs, and the rate of the expansion of the universe, we can determine the distance between them. Using the same method, the BAO signal can be traced back to its origins at the time of recombination. Since the standard cosmological model predicts the presence of BAOs in the universe, their discovery is more evidence for this theory. Due to the isotropy and homogeneity of the universe, we believe that any large sampled region of the universe is likely to contain BAO signals. We conclude that the method of the wavelet transformation first proposed by P. Arnalte-Mur [9] is not only sufficient to detect BAOs, but highly accurate. Cosmographer Brent Tully and Arnalte-Mur's method allowed us to detect BAO signals in the 2MRS for the first time, accurately determining their characterizing parameters and detecting their frequency.

Bibliography

- [1] M. Colless, “First results from the 2dF Galaxy Redshift Survey,” in *Large-Scale Structure in the Universe* (G. Efstathiou and et al., eds.), p. 105, 1999.
- [2] T. A. Moore, *A General Relativity Workbook*. University Science Books, 2013.
- [3] Z. Rostomian. Creative Services, Lawrence Berkeley National Laboratory.
- [4] J. P. Huchra, L. M. Macri, K. L. Masters, T. H. Jarrett, P. Berlind, *et al.*, “The 2MASS Redshift SurveyDescription and Data Release,” ApJS, vol. 199, p. 26, Apr. 2012.
- [5] É. Aubourg, S. Bailey, J. E. Bautista, F. Beutler, BOSS Collaboration, *et al.*, “Cosmological implications of baryon acoustic oscillation measurements,” Phys. Rev. D, vol. 92, p. 123516, Dec. 2015.
- [6] P. W., “Baryon acoustic oscillations: A cosmological ruler,” *Physics Today*, vol. 70, 2017.
- [7] B. R. Tully, “Galaxy Groups: A 2MASS Catalog,” *aj*, vol. 149, p. 171, May 2015.
- [8] G. Kaiser, *A Friendly Guide to Wavelets*. Birkhauser, 1994.
- [9] P. Arnalte-Mur, A. Labatie, N. Clerc, V. J. Martínez, J.-L. Starck, *et al.*, “Wavelet analysis of baryon acoustic structures in the galaxy distribution,” A&A, vol. 542, p. A34, June 2012.
- [10] A. A. Penzias and R. W. Wilson, “A Measurement of Excess Antenna Temperature at 4080 Mc/s.,” ApJ, vol. 142, pp. 419–421, July 1965.
- [11] A. Font-Ribera, D. Kirkby, N. Busca, J. Miralda-Escudé, N. P. Ross, *et al.*, “Quasar-Lyman α forest cross-correlation from BOSS DR11: Baryon Acoustic Oscillations,” J. Cosmology Astropart. Phys., vol. 5, p. 027, May 2014.
- [12] H.-J. Seo and D. J. Eisenstein, “Baryonic Acoustic Oscillations in Simulated Galaxy Redshift Surveys,” ApJ, vol. 633, pp. 575–588, Nov. 2005.

- [13] Kragh and H. Stjernholm, “Expanding earth and static universe : Two papers of 1935,” 2017.
- [14] J. S. Alin and C. L. Starr, *Undergraduate Matrix Theory and Linear Algebra*. CreateSpace Independent Publishing Platform, 2018.
- [15] A. Graps, *An Introduction to Wavelets*. University of Delaware.
- [16] J. R. Graham, *Convolution, Correlation, and Fourier Transforms*. 2009.
- [17] K. S. Dawson, D. J. Schlegel, C. P. Ahn, and e. a. Anderson, S. F, “The Baryon Oscillation Spectroscopic Survey of SDSS-III,” AJ, vol. 145, p. 10, Jan. 2013.